GEOPERSIA

Accepted Manuscript

Sparsity-based Regularization of Geophysical Time-domain Electrical Resistivity and Induced Polarization Data: A Strategy for Imaging Takhte-Gonbad Porphyry Cu Deposit

Mojtaba Hosseini, Maysam Abedi, MirSaleh Mirmohammadi, Reza Ghezelbash, Bardiya Sadraeifar

DOI: 10.22059/geope.2026.406213.648850

Receive Date: 13 November 2025
Revise Date: 26 April 2026
Accept Date: 04 June 2026

Sparsity-based Regularization of Geophysical Time-domain Electrical Resistivity and Induced Polarization Data: A Strategy for Imaging Takhte-Gonbad Porphyry Cu Deposit

Mojtaba Hosseini [1], Maysam Abedi [1], *, MirSaleh Mirmohammadi [1], Reza Ghezelbash [1], Bardiya Sadraeifar [2]

[1] School of Mining Engineering, College of Engineering, University of Tehran, Tehran, Iran
[2] Institute of Geophysics, University of Tehran, Tehran, Iran

Received: 13 November 2025, Revised: 26 April 2026, Accepted: 04 June 2026

Abstract
This research employs a combined geophysical approach, utilizing electrical resistivity tomography (ERT) and induced polarization (IP) imaging, to characterize the subsurface architecture and identify copper-bearing zones at the Takhte-Gonbad porphyry copper deposit within the Kerman metallogenic belt, Iran. The acquired field data were inverted using two distinct methodologies: conventional Tikhonov regularization and sparsity-based regularization. The resulting inverse models successfully delineated two principal E-W trending mineralized zones, which are distinguished by coherent low-resistivity and high-chargeability anomalies diagnostic of disseminated sulfide mineralization. These geophysical signatures exhibit a strong spatial correlation with surface-mapped zones of phyllic and argillic alteration and are further validated by borehole assay data confirming local copper grades exceeding 1%. A comparative assessment of the inversion results indicates that sparsity-based regularization produces subsurface models with sharper lithological boundaries and improved delineation of compact, high-contrast ore bodies, making it particularly effective for resolving localized features at the deposit scale. In contrast, Tikhonov regularization yields smoother models that are better suited for representing broader, regional-scale geological structures. Overall, both inversion approaches are capable of resolving the main subsurface features; however, they emphasize different aspects of the subsurface due to their inherent regularization properties. Accordingly, the choice between them should be guided by the geological objectives rather than interpreted as a general superiority of one method over the other.

Keywords: Sparsity-Based Regularization, Tikhonov Regularization, Geoelectrical Inversion, Takhte-Gonbad Deposit, Porphyry Cu.

Introduction

Mathematics plays a fundamental and essential role in solving geophysical inverse problems. Inverse problems are typically characterized by their nonlinear nature, non-uniqueness, and sensitivity to data noise, which necessitate the use of advanced mathematical and computational techniques (Jupp & Vozoff, 1975; Zhdanov, 2015; Aster et al., 2018; Wang et al., 2020). The investigation of geophysical challenges has led to the development of numerous mathematical models, whose successful applications have been demonstrated not only in Earth sciences but also across various other scientific disciplines. The evolution of diverse approaches in geophysical research gave rise to the theory of inverse problems, followed by the development of methods and algorithms designed to address the predominantly ill-posed nature of such

* Corresponding author e-mail: maysamabedi@ut.ac.ir

problems (Wang et al., 2020; Sadraeifar & Abedi, 2024). Geophysical inverse problems are intrinsically characterized by uncertainty and ill-posedness. Specifically, the use of limited and noise-contaminated observations frequently permits multiple viable model solutions, while minor perturbations in the measured data can induce substantial fluctuations in the reconstructed model. These inherent properties inevitably lead to non-unique inverse solutions that exhibit heightened sensitivity to data errors, often yielding disparate models capable of explaining the observed responses with comparable precision (Jupp & Vozoff, 1975; Zhdanov, 2015; Pallero et al., 2018; Fernández-Muñiz et al., 2019; Ren & Kalscheuer, 2020). The presence of equivalent models capable of reproducing the observed data with comparable misfit levels introduces significant ambiguity into the interpretation of the resulting solutions (Malinverno, 2002; Pallero et al., 2018; Fernández-Muñiz et al., 2019).

Regularization and optimization are essential mathematical tools in geophysical inversion for characterizing subsurface properties and geological structures. In this framework, the inverse problem is typically posed as the minimization of an objective function comprising a data fidelity term and a regularization term. The optimization process seeks to identify model parameters that both honor the observed data and adhere to the imposed regularization constraints (Gong et al., 2017; Benning & Burger, 2018; Luo et al., 2024; Sadraeifar & Abedi, 2024). Regularization incorporates prior constraints to stabilize ill-posed geophysical inverse problems arising from incomplete or noisy data, with the primary goal of yielding stable and physically meaningful solutions (Cheng et al., 2014; Bakushinsky et al., 2018; Benning & Burger, 2018; Sadraeifar & Abedi, 2024). Selecting the appropriate regularization form and parameters is crucial for balancing data fit against geological realism. Since many models can adequately explain the observations, the key task is to identify a solution that maintains this balance, respects prior information, and minimizes unwarranted complexity (Hong et al., 2017; Aster et al., 2018; Jordi et al., 2018; Sadraeifar & Abedi, 2024). Regularization directs model selection through norms that measure model complexity. A well-constructed regularization term encodes prior information and penalizes features like divergence from a reference model or sharp spatial gradients. Its minimization during optimization produces geologically plausible models that honor the data, effectively reducing non-uniqueness in inverse solutions (Jordi et al., 2018; Sadraeifar & Abedi, 2024). By introducing controlled smoothness or sparsity, regularization stabilizes inversions and prevents noise amplification. It also balances data fit against model simplicity (Silva et al., 2001; Aster et al., 2018). In practice, a penalty term added to the objective function discourages complexity and instability while preserving data consistency (Silva et al., 2001; Hong et al., 2017).

Among various regularization types, Tikhonov regularization is the most common in inverse problems. It adds a penalty term to the objective function to prevent overfitting, with the regularization parameter chosen globally or locally (Tikhonov, 1977; Golub et al., 1999; Wang et al., 2020; Gerth, 2021; Calvetti & Somersalo, 2025). This approach favors small parameter values, producing smooth, stable solutions that reduce noise and overfitting. It is especially suitable for media expected to exhibit gradual property variations (Fernández-Martínez et al., 2014; Toushmalani & Saibi, 2015; Sadraeifar & Abedi, 2024). Sparse regularization solves ill-posed inverse problems by seeking solutions where most coefficients are zero or near-zero, based on the premise that true models contain few significant features (Jin et al., 2017; Yu et al., 2023; Dai & Yin, 2025). The L1 norm (LASSO) is most common, driving parameters exactly to zero for simpler, interpretable models that avoid overfitting (Jin et al., 2017; Yu et al., 2023). Other norms (L0, L0-L1, L1-L2) offer greater flexibility and accuracy (Wang & Chen, 2022; G. Huang et al., 2024; Dai & Yin, 2025). This approach minimizes the number of non-zero parameters, making it well-suited for geological settings with few key features on a homogeneous background. Sparse regularization methods can, in some cases, provide a more focused representation of subsurface structures compared to L2-based solutions, particularly in the presence of sharp boundaries or compact anomalies(Grasmair et al., 2015; Sadraeifar & Abedi, 2024). Although porphyry copper systems are not strictly sparse in a mathematical sense, as they commonly exhibit gradational alteration halos and disseminated mineralization, the use of sparsity-promoting regularization in this study does not assume an inherently sparse geological structure. Instead, it is employed as a modeling strategy to enhance the recovery of localized, high-contrast features that are typically associated with mineralized zones, such as sulfide-rich cores characterized by elevated chargeability or sharp resistivity contrasts linked to structural controls. In this framework, L0/L1-based regularization helps suppress excessive spatial smearing and improves the delineation of compact anomalies, even in geological settings that involve both gradual and abrupt spatial variations. Additional regularization approaches include variational/nonlinear methods (useful for image processing and nonlinear problems; Cheng et al., 2014; Benning & Burger, 2018; Bredies & Holler, 2020); Bayesian regularization (incorporating prior information statistically, equivalent to posterior maximization, including Horseshoe, Lasso, and Ridge; Català & Angulo, 2000; Aster et al., 2018; Sadraeifar & Abedi, 2024); Total Variation regularization (preserving edges and discontinuities, valuable for seismic and electromagnetic imaging; Gholami & Hosseini, 2013; Strong & Chan, 2003; Lima et al., 2011; Lin & Huang, 2015; Gupta et al., 2018; Bredies & Holler, 2020; Sadraeifar & Abedi, 2024); and polynomial/composite regularization (combining multiple terms for complex problems; Xu et al., 2017; Bortolotti et al., 2025).

Regularization methods improve mineral inversion accuracy and efficiency. This study compares Tikhonov and sparse regularization. Tikhonov regularization, established in the 1960s (Bauer et al., 2007; Doicu et al., 2010; Gockenbach, 2016), is widely used but suffers from excessive smoothing that blurs sharp geological boundaries. This limitation spurred sparse regularization, which emerged in the 1990s via Basis Pursuit and LASSO using L1/L0 norms (Wright et al., 2009; Duval & Peyré, 2017; Zheng et al., 2018; Li, 2023). Subsequent algorithmic developments (e.g., iterative thresholding, gradient-based, reweighted schemes) and extensions to non-convex regularizations (Lp norms, combinations with TV or group terms) have further enhanced accuracy and flexibility (Hu et al., 2017; Selesnick, 2017; Wen et al., 2018; Hassan Ibrahim et al., 2020; Tang et al., 2022; Li, 2023). Case studies confirm that diverse regularization methods enable more accurate mineralized zone identification and reduced subsurface ambiguity. In 2024, Sadraeifar and Abedi compared Tikhonov and sparsity-promoting regularization methods on gravity data. Their results showed that Tikhonov regularization yielded smoother and more uniform models, whereas sparsity-promoting approaches produced models with sharper boundaries and more localized features associated with mineralization. Additionally, Zhong et al. (2021) applied L0, L1, and L2 norm regularizations to electrical resistivity data, showing that sparsity-promoting approaches (L0 and L1) can improve the delineation of targets with sharp boundaries compared to Tikhonov (L2) regularization (Zhong et al., 2021; Sadraeifar & Abedi, 2024).

Northwestern Kerman Province is one of the richest porphyry copper mineralization regions in Iran, where the Sirjan mineralized area has been extensively investigated through the analysis of exploration data in several studies (Afzal et al., 2016; Hosseini et al., 2017; Babaei et al., 2020; Babaei et al., 2021; M.-L. Huang et al., 2024). Among the numerous copper deposits in this region, the Takhte-Gonbad porphyry copper deposit has been selected as the case study in this research to investigate the porphyry copper mineralization using geophysical data inversion with two regularization methods. The Takhte-Gonbad mineralized area is located 15 km northeast of the Chahar-Gonbad vein-type mine and is predominantly covered by Eocene volcanic-sedimentary rocks (Hosseini, 2012). In this study, inversion of electrical resistivity and induced polarization (IP) data was performed using Tikhonov and sparsity-promoting regularization methods. The primary objective of the Tikhonov inversion was to obtain a model that balances data misfit and model smoothness, while the sparsity-promoting inversion was designed to encourage compact model structures and to improve the delineation of potential porphyry copper zones, particularly in the presence of sharp or localized anomalies. The performance of both regularization methods was evaluated for synthetic and real field data in terms of recovering the geometry and depth of a mineralized body. The geophysical inversion was carried out using the open-source SimPEG library (version 0.24.0), which is a powerful tool for parameter estimation (Cockett et al., 2015). The modeling and inversion were conducted on an ASUS laptop with an Intel® Core™ i7-13620H processor at a base frequency of 2.4 GHz and 32 GB of RAM.

Geological Setting

The Urumieh–Dokhtar magmatic belt (UDMB) in Iran is one of the world's major copper-bearing regions. Most of the discovered copper deposits along this belt are located in the Cenozoic magmatic arc of Kerman, many of which display characteristics of porphyry-type deposits. This belt, trending northwest–southeast, extends approximately 400 km in length and 40–50 km in width along the southern margin of the Central Iran block. In the Kerman region, copper mineralization is concentrated in several major porphyry copper deposits, representing the prospectivity of the Cenozoic magmatic complex of Kerman (Shafiei et al., 2009). Most of the known porphyry deposits are located in the southern part of this belt, commonly referred to as the Kerman belt (KB) (Hosseini et al., 2017).

The Takhte-Gonbad deposit, located in the southwestern part of the KB, comprises Eocene volcanic–sedimentary rocks and Late Eocene–Early Oligocene red sedimentary rocks that have undergone intense metamorphism, thermal metamorphism, and hydrothermal alteration. Two main lithological assemblages with diverse mineralogy–tuffs, sandstones, and skarns—have been identified; in contact with Oligocene intrusive and granodiorite units, these rocks have been metasomatized and mineralized. The intrusive units in the area include a granitic batholith, porphyritic granodiorite, and post-mineralization rhyodacite–dacite dikes. The predominant faults and fractures trend southeast and northeast, exerting a controlling influence on the structure and porphyry copper mineralization. The Takhte-Gonbad deposit, of Oligocene age and magmatic origin related to a subduction environment, has been affected by potassic, phyllic, and propylitic hydrothermal phases, which controlled the formation of quartz–magnetite–chalcopyrite veins and veinlets within the host rocks. Structural studies indicate that these deposits predominantly formed in local extensional zones under a compressive–transpressive regime, with stress fields and faults playing a key role in fluid flow and ore deposition (Hosseini et al., 2017; Tinooni, 2021; M.-L. Huang et al., 2024). Fig. 1 shows the location of the study area on the structural geological map of Iran.

The main lithological units within the mineralized zone comprise a sequence of volcaniclastic rocks, intrusive bodies, sedimentary sequences, and skarn. The tuff units in the mineralized area can be subdivided into two main groups based on their degree of alteration by porphyry intrusions associated with mineralization. Crystal tuffs of white-green to gray colors, along with tuffaceous limestones and tuffites, occur in contact with intrusive bodies and have undergone extensive silicification and hornfelsing, being closely associated with high-grade mineralization. The lithology of this unit is relatively diverse, including lithic tuff, tuffite, vitric tuff, crystal-lithic tuff, and shale tuffs with intercalations of carbonates. Owing to the initially high porosity of this unit, widespread alteration facilitated the infiltration and circulation of ore-bearing fluids derived from microgranodioritic intrusions, thereby promoting mineralization. Chalcopyrite, accompanied by pyrite and magnetite, occurs in disseminated grains and veinlets, frequently associated with silica stockworks. Distinctive features of mineralization in this unit include fine-grained disseminated chalcopyrite (average size 30–40 μm), relatively high copper grades (up to 2%), and abundant magnetite. Oxidation processes transformed iron sulfides such as pyrite and chalcopyrite into iron oxides and hydroxides, which accumulated within fractures and fissures. Secondary copper carbonates, including malachite and azurite, are abundantly developed along these fractures (Hosseini et al., 2012). Fig. 2 presents the 1:5,000 map of the study area, showing the geoelectric survey lines along with the locations of exploration drill holes.

Porphyry-type copper mineralization occurs as veins, veinlets, and disseminations within thermally altered and skarnified pyroclastic rocks, as well as within porphyritic intrusive bodies (Hosseini et al., 2017; Mohammadi & Hezarkhani, 2018). Phyllic, propylitic, silicic, and carbonate alterations are sporadically observed in the study area, among which the phyllic alteration shows the widest extent and highest intensity, particularly within tuffs and microgranodioritic intrusions. This type of alteration is directly associated with hypogene copper mineralization and is characterized by sericite (muscovite and illite), quartz, minor chlorite, pyrite, and chalcopyrite (Babaei et al., 2021). Argillic or intermediate argillic alteration is recognized as the most widespread and common type of alteration in many porphyry copper systems (Ranjbar et al., 2004; Fakhari et al., 2019). This type of alteration results from the alteration of plagioclase and produces minerals such as kaolinite, illite, smectite, and montmorillonite. Argillic alteration is widely observed in surface exposures and at shallow depths. Propylitic alteration also occurs along irregular margins surrounding the core of the deposit and is characterized by the presence of chlorite, calcite, epidote, and minor amounts of zeolite and amphibole (Hosseini et al., 2017; Mohammadi & Hezarkhani, 2018).

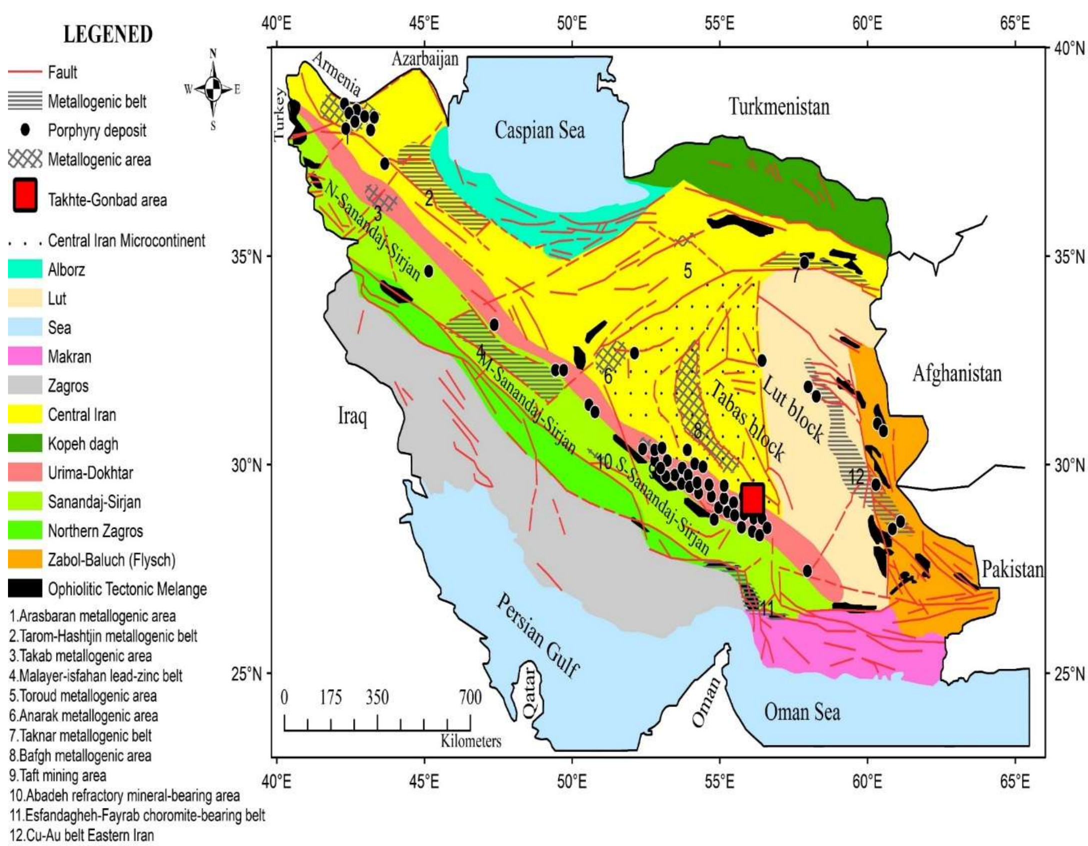

Figure 1. The distribution map of porphyry Cu deposits (black dots) over the structural geology map of Iran, where the study area indicated by a red square in the south of the Urumieh-Dokhtar magmatic belt (UDMB)

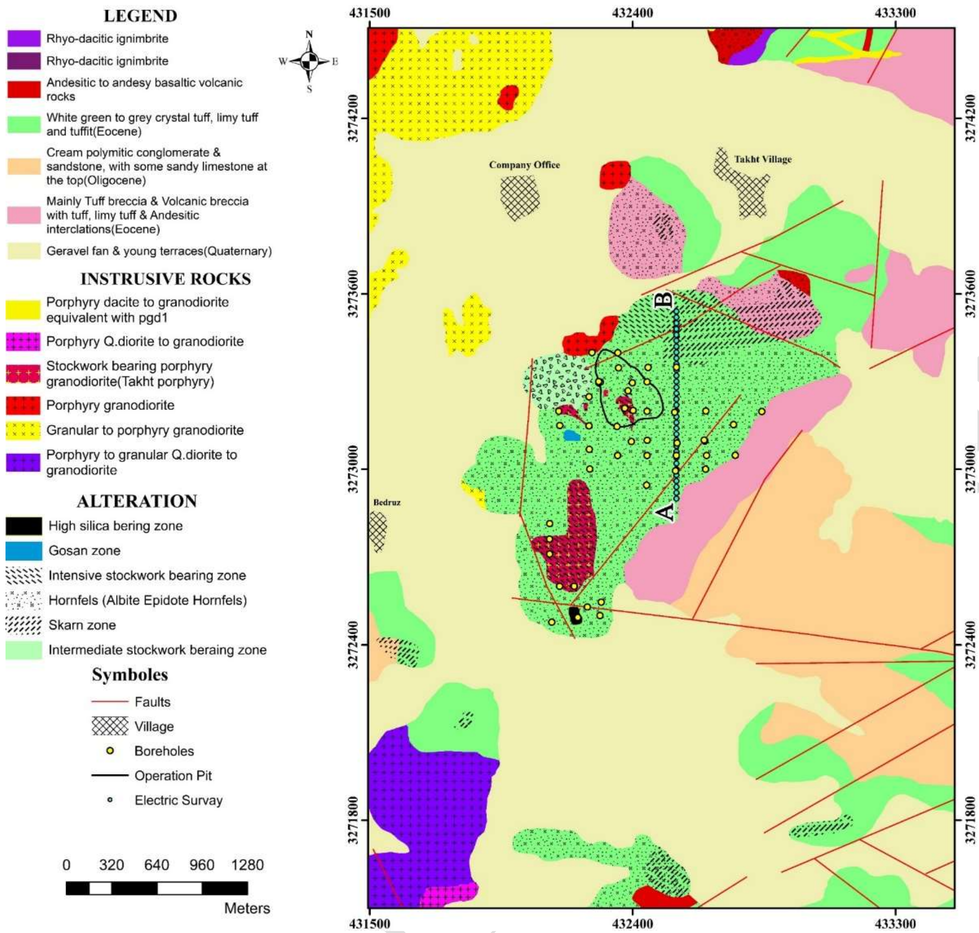

Figure 2. A simplified geological map of the Takhte-Gonbad area at a scale of 1:5,000, showing the locations of the 2D ERT and IP profiles, along with the positions of the boreholes

Chalcopyrite is the principal ore mineral in the hypogene zone, occurring together with pyrite and minor magnetite along veinlets, particularly within granodiorite and tuff units. The economic grade of copper in the hypogene zone has been identified at approximately 150 meters below the oxidized cap (Hosseini et al., 2012; Afzal et al., 2016). In the oxidized zone, chalcopyrite has been altered to copper carbonates such as malachite. In the Takhte-Gonbad deposit, mineralized sections have developed within a transitional zone between the hypogene, immature supergene, and oxidized zones. The thickness of the supergene enrichment zone varies between 10 and 50 meters and is predominantly composed of chalcocite and covellite (Hosseini et al., 2012; Hosseini et al., 2017). The study area is located within an active tectonic setting, controlled by right-lateral strike-slip structures and intersected in the southern part by the Naein–Baft and Chahar-Gonbad faults. Surface geological evidence indicates that the copper deposit is predominantly oriented east–west rather than north–south (Hosseini et al., 2012; Mohammadi & Hezarkhani, 2018).

Methodology

Forward Modelling

In geophysics, the forward problem is considered a fundamental aspect, which involves calculating the responses based on assumed sources and known Earth models. This relationship is expressed as follows:

$$F_j[m] = d_j^{obs} \equiv d_j + n_{j,} \quad j = 1, \dots, N \tag{1}$$

Here, F_j represents the forward modeling operator, which incorporates the detailed survey design and the relevant physical equations. The symbol m typically denotes the distribution of physical properties, while the right-hand side of the equation represents the observed data d_j^{obs}, composed of the true data $d_j$and added noise n_j. The operator F can take various forms, often appearing in integral or differential formulations that require numerical methods for their solution. Despite challenges such as the high computational demand for modeling electromagnetic responses in a three-dimensional Earth, the forward modeling problem is considered a well-posed problem, having a unique solution (Oldenburg & Li, 2005). Understanding the forward problem is an integral part of geophysical exploration and plays a key role in the development of inversion algorithms (Chen & Zhang, 2018). The inversion process is based on solving the forward problem, where data are calculated from a given set of model parameters. Although it is typically assumed in inverse problems that the forward solution is fully known, in practice its implementation through the forward modeling process is inherently prone to errors; these are referred to as modeling errors (Hansen et al., 2014).

In the following, the mathematical formulation necessary for forward modeling of time-domain electrical resistivity is briefly outlined. This modeling is based on the numerical solution of the electrostatic Poisson equation for the electric potential. To obtain a numerical solution of this partial differential equation, the continuous domain must be discretized into a mesh, and the equations are converted into an algebraic form (matrix system). This discretization is performed using the finite-volume method on a staggered mesh, where the conductivity is defined at cell centers, the current density on cell faces, and the electric potential at cell centers.

$$\nabla \cdot (-\sigma \nabla \phi) = I\big(\delta(\vec{r} - \vec{r}_{s^+}) - \delta(\vec{r} - \vec{r}_{s^-})\big) = q \tag{2}$$

In this equation, σ represents the electrical conductivity, ϕ is the electric potential, and I denotes the injected current applied at the positive and negative locations of the dipole ($\vec{r}$), which are modeled using Dirac delta functions to represent point-source behavior. To implement the continuous equations computationally, the subsurface must be discretized to represent it with a finite set of values. This discretization allows spatial derivatives to be approximated using central differences, resulting in a second-order accurate stepwise discretization. Equation (2) relates the divergence of the current density to the source term. For the finite-volume discretization, the divergence is considered in a geometric sense as follows:

$$v \, \mathrm{Dj} = q \tag{3}$$

Here, v represents the volume (or area) of the cell, D is the discrete divergence operator matrix, j is the vector of current density on the cell faces, and q denotes the discretized source term (Cockett et al., 2016).

The discretization of the inner product on cell faces can be represented by an abstract function $\mathrm{M}_f(\sigma^{-1})$, which applies the inner product across the entire mesh in a single operation. By defining the necessary operators over the full mesh, two discrete equations remain.

$$\mathrm{diag(v)Dj = q} \tag{4}$$

$$\mathrm{M}_f\ (\sigma^{-1})\mathrm{j} = \mathrm{D}^{\intercal}\mathrm{diag(v)}\phi \tag{5}$$

At this stage, all variables are defined over the entire mesh. The coupled system can either be solved directly, or the current density **j** can be eliminated to solve directly for the potential ϕ, resulting in a smaller, second order system.

$$\mathrm{diag(v)DM}_f(\sigma^{-1})^{-1}\mathrm{D}^{\intercal}\mathrm{diag(v)}\phi = \mathrm{q} \tag{6}$$

By solving this system matrix, a response for the electric potential ϕ is obtained throughout the entire domain. To generate the predicted data from this response, the potential values are interpolated to the electrode positions, and the potential differences between the corresponding electrodes are then computed (Cockett et al., 2016).

In this study, in addition to the forward modeling of electrical resistivity, IP forward modeling was also performed to characterize subsurface chargeability features. In this model, the electrical conductivity of the medium is represented by σ(**r**) and its chargeability by η(**r**), both of which are spatially dependent functions within the subsurface. The direct current (DC) potential field generated by the injection of a unit current at position $\mathbf{r}_s$ is described by the following partial differential equation:

$$\nabla \cdot (\sigma \nabla \phi_\sigma) = -\delta(\mathrm{r} - \mathrm{r}_s) \tag{7}$$

In this equation, ϕ_σ denotes the potential in the absence of IP effects. When the medium exhibits a nonzero chargeability ($\eta \neq 0$), this property effectively reduces the electrical conductivity by a factor of $(1 - \eta)$ (Seigel, 1959). Consequently, the total potential ϕ_η in the presence of IP effects can be expressed as follows:

$$\nabla \cdot \big(\sigma(1-\eta)\nabla \phi_\eta\big) = -\delta(\mathrm{r} - \mathrm{r}_s) \tag{8}$$

The difference between the calculated potentials in the two cases — with and without the IP effect — is defined as the secondary potential:

$$\phi_s = \phi_\eta - \phi_\sigma \tag{9}$$

Furthermore, the apparent chargeability, which is commonly used in IP survey data interpretation, is defined as follows:

$$\eta_a = \frac{\phi_\eta - \phi_\sigma}{\phi_\eta} \tag{10}$$

Apparent chargeability represents the preferred form of IP data and is well-defined in both some surface and borehole surveys (Li & Oldenburg, 2000).

Inversion Methodology

Li and Oldenburg define geophysical inversion as an optimization problem, which can generally be expressed as follows (Li & Oldenburg, 1996, 2003):

$$\min \phi(m) = \phi_d + \beta \phi_m \tag{11}$$

where $\phi(m)$ acts as the objective function, consisting of two main components: the data misfit term ϕ_d, which measures how well the model m fits the observed geophysical data, and the regularization term ϕ_m, which imposes constraints to control the inherent complexity and non-uniqueness of the inversion model. Finally, the parameter β balances the relative contributions of ϕ_d and ϕ_m in the total objective function $\phi(m)$ (Li & Oldenburg, 1996, 2003). The data misfit term ϕ_d is defined as the sum of the squared differences between the observed data $\left(d_i^{obs}\right)$ and the predicted data $\left(d_i^{pre}\right)$ and is generally expressed as (Ardestani et al., 2022):

$$\phi_d = \sum_{i=1}^{N} \left(\frac{d_i^{pre} - d_i^{obs}}{\varepsilon_i}\right) = \|W_d(F(m) - d^{obs})\|_2^2 \tag{12}$$

Here, ε_i represents the estimated uncertainty or standard deviation associated with each data point. W_d is a diagonal weighting matrix whose entries are the inverse of the data uncertainties. $F(m)$ is a nonlinear projection matrix that relates the electrical model parameters m to the predicted data d_i^{pre}. This formulation quantifies the misfit between the observed and predicted data while accounting for the individual uncertainties ε_i of each observation (Li & Oldenburg, 1996, 2003; Ardestani et al., 2022).

In the context of regularization, the Tikhonov method is expressed as follows (Li & Oldenburg, 1996; Ardestani et al., 2022):

$$\phi_m = \alpha_s\phi_s + \alpha_x\phi_x + \alpha_y\phi_y + \alpha_z\phi_z = \sum_{r=s,x,y,z} \alpha_r \left\| W_r V_r G_r (m - m^{ref}) \right\|_2^2 \tag{13}$$

The term ϕ_s represents the smallness component, while $\phi_{x,y,z}$ denote the roughness components. The smallness term quantifies the deviation of the recovered model from a reference model, effectively constraining the model parameters to remain close to a set of prior values. In contrast, the roughness terms measure the smoothness of the model in different spatial directions (typically along the Cartesian axes x, y and z). The matrices $W_{r(s,x,y,z)}$, $V_{r(s,x,y,z)}$ and $G_{r(s,x,y,z)}$ have significant impact on the regularization of the model objective function (Eq. 11). $W_{r(s,x,y,z)}$ are depth weighting matrices that assign specific weights to different parts of the model or data, reflecting their relative importance or reliability. $V_{r(s,x,y,z)}$ are introduced as volumetric weighting matrices that normalize the contributions of different model cells according to their size, ensuring balanced representation. $G_{r(s,x,y,z)}$ are gradient operators that measure the directional derivatives of the model parameters. Overall, the inclusion of smallness and roughness components helps to avoid overfitting, ensures model stability, and guides the inversion toward geologically realistic solutions by incorporating prior knowledge and spatial regularization (Li & Oldenburg, 2003).

The sparsity regularization term is represented as follows:

$$\phi_m = \sum_{r=s,x,y,z} \alpha_r \left\| W_r V_r G_r (m - m^{ref}) \right\|_{0\ or\ 1} \tag{14}$$

The ℓ_0 (or ℓ_1) norm is used to encourage sparsity in the model parameters. The Sparse regularization term penalizes the absolute values of the elements of $W_r V_r G_r (m - m^{ref})$ instead of their squared values, promoting sparsity in the solution (Gholami & Siahkoohi, 2010). The choice between these regularization techniques affects the characteristics of the recovered model. Tikhonov regularization tends to produce smooth solutions, whereas sparse regularization promotes sparsity in the solution (Sadraeifar & Abedi, 2024). Regarding the ℓ_0 regularization term in Eq. (14), it is noted that exact ℓ_0 minimization is a non-convex, NP-hard optimization problem and is therefore intractable in practice. In this study, the ℓ_0 norm is approximated using an iterative reweighted least squares (IRLS) framework, which provides a surrogate formulation for promoting sparsity in the model parameters. Within this framework, the optimization is carried out iteratively, with model-dependent weights updated at each iteration based on the current solution. This procedure progressively enhances sparsity throughout the inversion process. The IRLS approximation offers a computationally efficient and stable surrogate to the ℓ_0 norm while retaining its ability to recover compact, high-contrast anomalies. The inversion is terminated based on a maximum number of IRLS iterations together with convergence criteria in terms of data misfit and model updates, ensuring stability of the final solution. For 2D modeling along the north–south direction, the x component in Eq. (14) can be omitted, and the regularization term can be rewritten as follows:

$$\phi_m = \alpha_s \left\| W_s V_s G_s (m - m^{ref}) \right\|_{0\ or\ 1} + \alpha_y \left\| W_y V_y G_y (m - m^{ref}) \right\|_{0\ or\ 1} + \alpha_z \left\| W_z V_z G_z (m - m^{ref}) \right\|_{0\ or\ 1} \tag{15}$$

The choice between these regularization techniques influences the characteristics of the recovered model. Tikhonov tends to produce smooth solutions, while Sparse encourages sparsity in the solution.

The reference model m^{ref} in Eq. (13–15) is defined as a homogeneous background model. A constant value, representing the expected average subsurface properties, was assigned uniformly to all cells of the computational mesh. This is a standard assumption in geophysical inversion when reliable priori geological information is not available. The resulting homogeneous model provides a neutral starting point from which deviations are recovered during inversion. Within the sparsity-promoting regularization framework, the reference model defines the baseline relative to which model perturbations are estimated. Using a constant reference model ensures that sparsity is imposed on deviations from a uniform background, rather than from a spatially varying prior. The same reference model was used in both the Tikhonov and sparsity-promoting inversion schemes to ensure consistency between the two approaches. Accordingly, m^{ref} corresponds to a homogeneous half-space and does not incorporate any spatially varying prior information. Alternative choices, such as spatially varying reference models, may influence sparsity-based results; however, they were not considered here in order to maintain a controlled and consistent comparison of regularization strategies.

To account for the natural decay of sensitivity with depth in ERT/IP inversion, a sensitivity-driven depth-weighting scheme, as implemented in the SimPEG framework, was applied. Specifically, the UpdateSensitivityWeights() routine was used to compute model weights from the diagonal elements of the sensitivity (Jacobian) matrix. This formulation assigns lower weights to shallow cells with high sensitivity and relatively higher weights to deeper cells, thereby compensating for the inherent bias of inversion results toward near-surface structures. Depth weighting plays a key role in stabilizing the inversion and enabling deeper regions to contribute meaningfully to the recovered model. Without such weighting, both smooth and sparsity-promoting inversions tend to concentrate on anomalies near the surface due to the rapid decay of data sensitivity with depth. In this study, the same sensitivity-based depth-weighting scheme was applied consistently to both the Tikhonov and sparsity-promoting inversion frameworks. This ensures that any differences between the resulting models arise from the choice of regularization rather than inconsistencies in sensitivity compensation. Although depth weighting influences the overall distribution of recovered parameters, it is applied uniformly across both approaches and therefore does not bias the comparative analysis. Instead, it provides a consistent basis for evaluating the relative performance of smooth and blocky regularization. The inversion is performed using a projected Gauss–Newton conjugate gradient (GNCG) optimization scheme. Multiple stopping criteria are used to ensure stability and consistency of the recovered model. Specifically, the inversion is terminated when the data misfit reaches the expected noise level. Within the iterative reweighted least squares (IRLS) framework, convergence is additionally monitored through the relative change in the objective function. The IRLS iterations are stopped when this change falls below a prescribed threshold (10^{-4}) or when a maximum of 40 iterations is reached, whichever occurs first. An overall maximum iteration limit is also enforced as a safeguard. These criteria collectively ensure a controlled inversion process, preventing overfitting while maintaining consistency with the assumed noise characteristics of the data.

Geophysical survey

For the geoelectrical surveys in this study, one selected profile was used that effectively intersected the existing boreholes. In the study area, efforts were made to design and implement the survey lines as perpendicular as possible to the mineralization veins and geological structures. Accordingly, data acquisition was conducted along profiles oriented in the north–south direction. The measurements were carried out over the specified area using a Scintrex IPR12 instrument manufactured in Canada. Each electrical survey profile was 660 meters long, and grid positioning was performed using Garmin Vista and Garmin Map 60CSx GPS devices.

The pole–dipole array was selected for data acquisition, as it allows for greater investigation depth, higher field efficiency, and faster data collection—considering both the mineralization depth and field conditions. The surveys were conducted with an electrode spacing of 40 meters and 15 skips with an interval of 20 meters. The resistivity and IP methods were chosen due to their strong capability in detecting sulfide mineralization and certain metallic oxides such as magnetite. IP data can indicate the presence of sulfide minerals (e.g., pyrite and chalcopyrite), particularly in zones exhibiting high chargeability.

Synthetic Scenarios

In geophysical exploration, the choice of a regularization method can have a significant impact on the quality and accuracy of inversion results. To demonstrate this effect, a forward-modeling study was carried out to evaluate the performance of both Tikhonov and sparse regularization approaches in reconstructing simple subsurface features of electrical resistivity and chargeability. For the synthetic model, an artificial domain with dimensions of 500 × 250 meters was discretized into a grid of 130 × 62 cells, each measuring 5 meters in size. The horizontal axis (y) extended from 0 to 500 meters, while the vertical axis (z) ranged from 0 to –250 meters. In both models, a rectangular body of 100 × 50 meters was defined to represent a sulfide zone bearing copper, and four smaller rectangular bodies of 50 × 25 meters were introduced to simulate silicified zones bearing copper mineralization. In the resistivity modeling, a background resistivity of 100 Ω·m was assumed, while the sulfide zone and the silicified zone were assigned resistivity values of 20 Ω·m and 500 Ω·m, respectively (Fig. 3a). In the chargeability modeling, a background chargeability of 5 mV/V was used, with 50 mV/V assigned to the copper-bearing sulfide zone and 30 mV/V to the silicified copper-bearing zone (Fig. 4a). Synthetic resistivity and chargeability data were contaminated with 2% Gaussian noise to simulate realistic field conditions.

The main objective was to accurately reconstruct the characteristics of the two copper-bearing zones - including their geometry, resistivity, chargeability, and depth — using geoelectrical inversion methods. Distinct weighting schemes were employed for the two inversion methods. The Tikhonov regularization utilized equal weights ($\alpha_{s,y,z} = 1$) for both the smallness and smoothness constraints in the resistivity and chargeability inversions. In contrast, the sparse regularization applied a strongly asymmetric weighting ($\alpha_s = 0.01, \alpha_{y,z} = 1$) to penalize the smallness term minimally and the smoothness term significantly, thereby promoting sparse, blocky solutions that preserve subsurface boundaries. The inversion results indicate noticeable differences between the two regularization approaches. The Tikhonov inversion produced smoother models and showed some limitations in resolving the depth extent of the copper-bearing zones (Fig. 3b and Fig. 4b). In contrast, the sparsity-promoting inversion yielded more focused models, with improved delineation of the geometry of the copper-bearing zones, particularly in terms of boundary definition (Fig. 3c and Fig. 4c). By promoting compact structures and reducing spatial smearing, the sparsity-based approach enhances the representation of key features in the data. However, its performance is dependent on the underlying model characteristics and may not necessarily provide more accurate estimates of bulk physical property values.

The Tikhonov regularization is designed to promote solutions in which all model parameters remain small, though not necessarily sparse. This inherent tendency toward smoothness can sometimes blur sharp subsurface boundaries and make the precise determination of the depth of mineralized zones more difficult. Figs. 5a and 5b display the synthetic observed resistivity and chargeability data, respectively. Figs. 5c and 5e present the predicted chargeability data obtained from the inversion of the synthetic model using the Tikhonov and sparse regularization methods. Similarly, Figs. 5d and 5f illustrate the predicted resistivity data derived from the inversion of the synthetic model with the same two regularization schemes. A comparison of the results obtained from the two regularization methods indicates that sparsity-promoting inversion yields more focused model recovery with reduced spatial smearing relative to the Tikhonov approach, particularly in resolving compact or high-contrast features. These differences should, however, be interpreted with caution, as the performance of each method depends on the underlying model characteristics and inversion parameters. Accurate recovery of the dip of the assumed silica structure (Figs. 3c and 4c) would likely require additional structural constraints. While the incorporation of such prior information could further improve the inversion results, this aspect is beyond the scope of the present study.

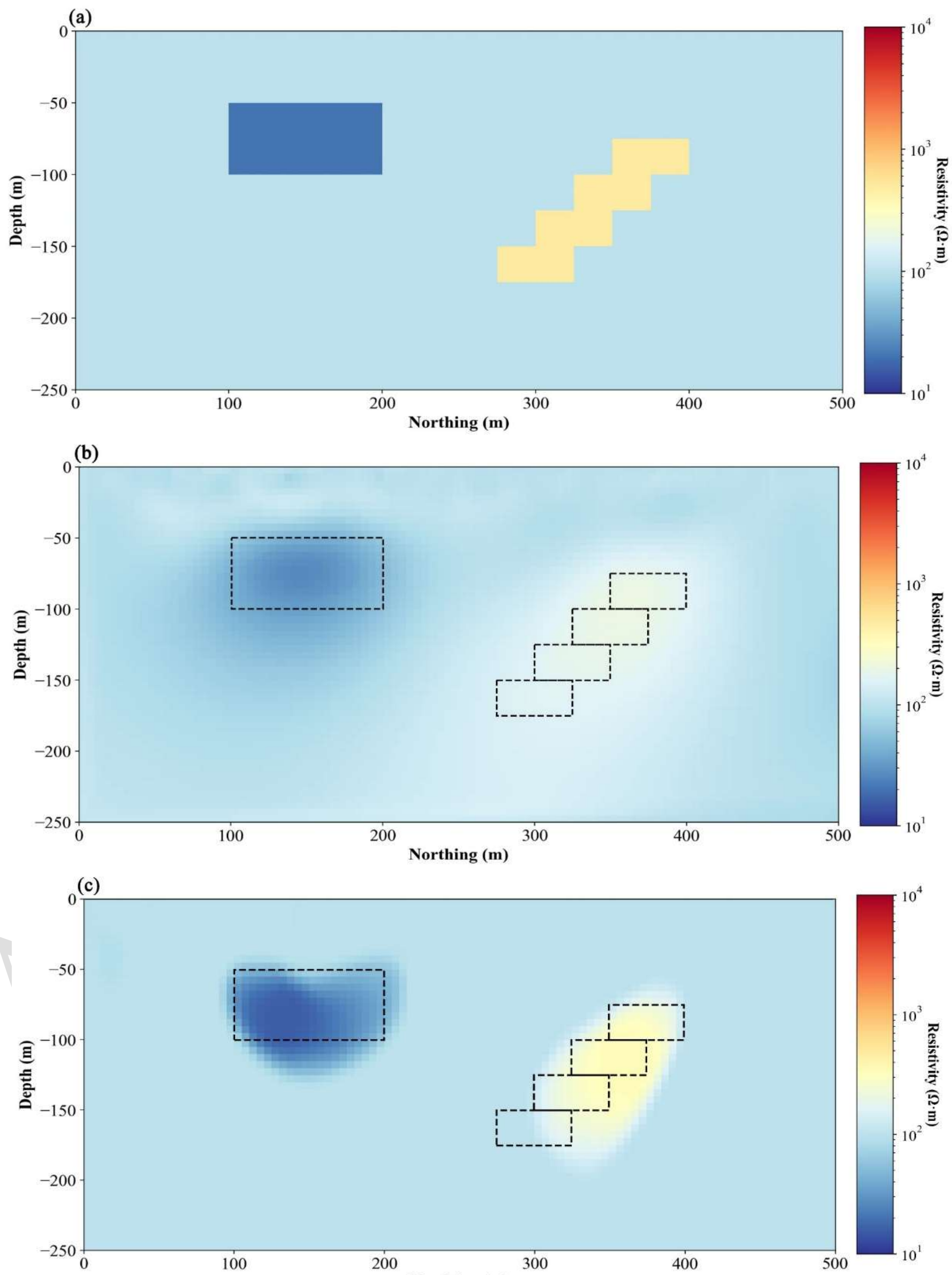

Figure 3. Synthetic electrical resistivity data modeling, (a) True electrical resistivity model, (b) result of inversion by the Tikhonov regularization, (c) result of inversion by the Sparse regularization

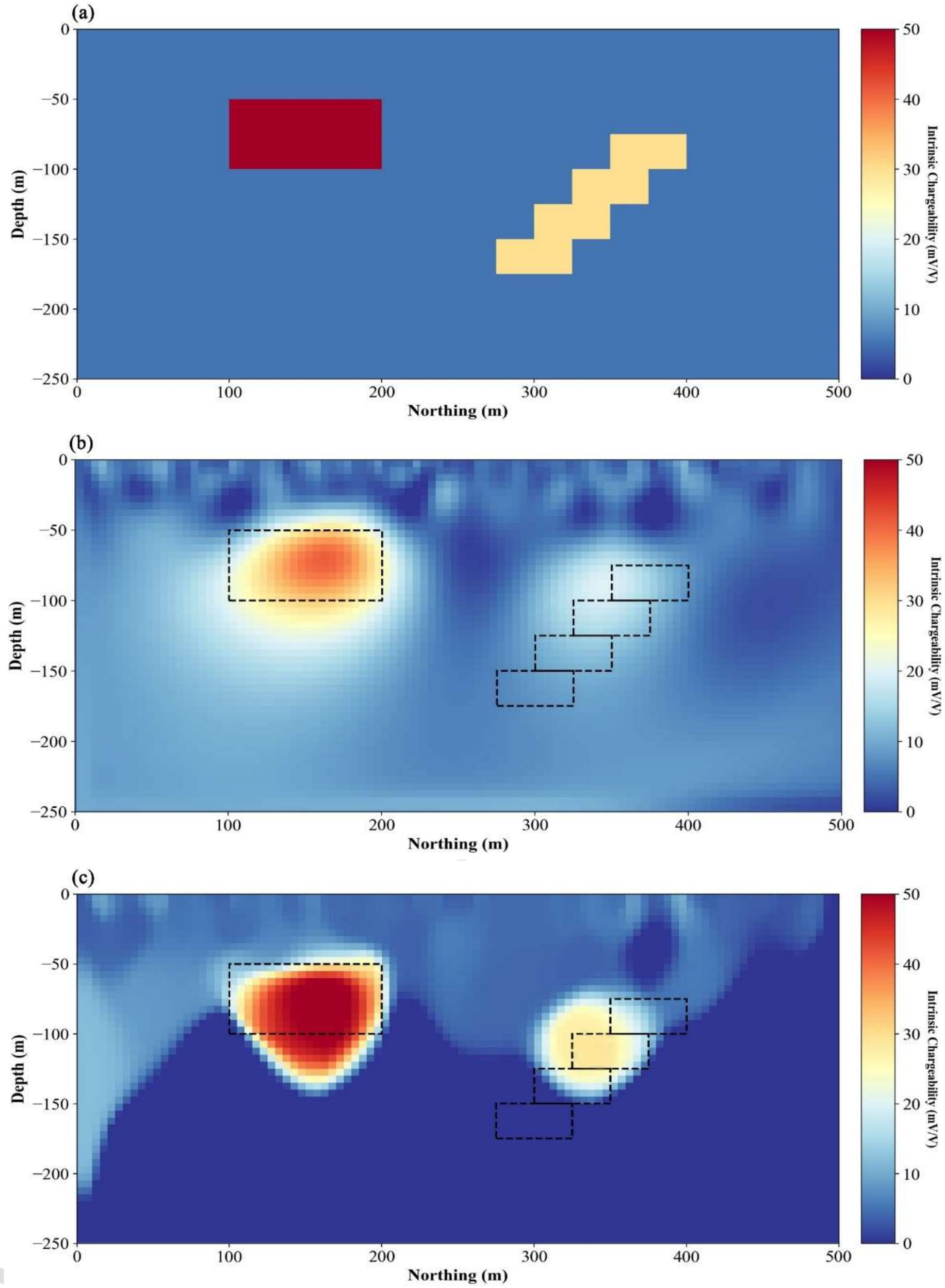

Figure 4. Synthetic electrical chargeability data modeling, (a) True electrical chargeability model, (b) result of inversion by the Tikhonov regularization, (c) result of inversion by the Sparse regularization

Inversion of Real Geoelectrical Data

For quantitative interpretation and inversion of the geoelectrical data acquired along profile A–B, a two–dimensional inversion was performed using both Tikhonov and sparse regularization methods. In the Tikhonov approach, equal weighting factors of 1 were applied to the smallness and smoothness terms for both resistivity and chargeability inversion promoting smooth and continuous model variations $(\alpha_{s,y,z} = 1)$. In contrast, the sparse regularization assigned a weight of 0.01 to the smallness term and 1 to the smoothness term encouraging sparse and edge-preserving solutions while emphasizing essential subsurface features$(\alpha_s = 0.01, \alpha_{y,z} = 1)$.

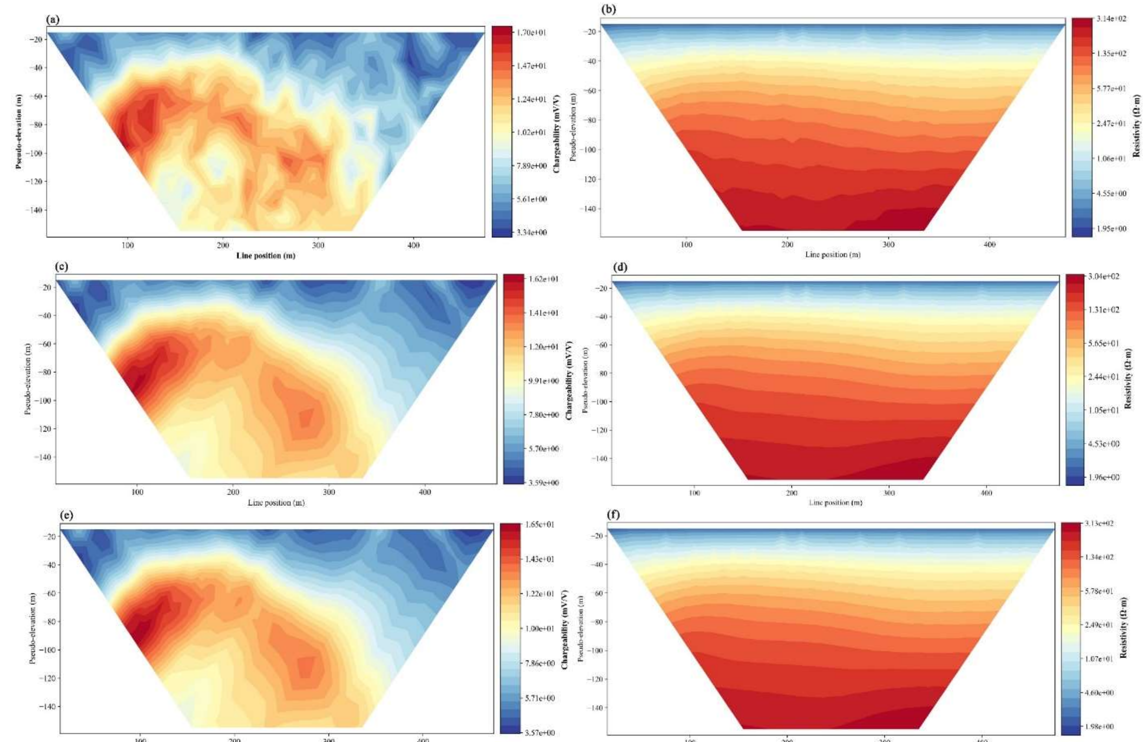

Figure 5. (a) Synthetic apparent chargeability data, (b) Synthetic apparent electrical resistivity data, (c) Synthetic predicted apparent chargeability data with Tikhonov regularization, (d) Synthetic predicted apparent electrical resistivity data with Tikhonov regularization , (e) Synthetic predicted apparent chargeability data with Sparse regularization, (f) Synthetic predicted apparent electrical resistivity data with Sparse regularization

Additionally, for the smallness term and the spatial gradients along the y and z directions, the norms were set to $[0,2,2]$, respectively. In the resistivity inversion, the lower and upper bounds of the model parameters were set to 10 Ω·m and 10,000 Ω·m, respectively, while in the chargeability inversion, the lower and upper bounds were defined as 0 mV/V and 50 mV/V, based on a comprehensive assessment of geological data and borehole information to ensure that the inversion results are consistent with the actual subsurface conditions. Fig. 2 presents a 1:5000-scale map of the study area, showing the geoelectrical survey profile and exploratory boreholes.

The inversion of field geoelectrical data was performed on a subsurface domain discretized into a 280 × 120 cell TensorMesh. Observed resistivity and chargeability data are presented in Figs. 6a and 6b, respectively. The corresponding predicted data from the Tikhonov and sparse regularizations are shown in Figs. 6c–6f. The resistivity inversions for both methods converged within 20 iterations. In contrast, the chargeability inversion required 11 iterations with Tikhonov regularization and 50 iterations with sparse regularization to achieve convergence.

Fig. 7 presents the inversion results of electrical resistivity and chargeability along profile A–B. The results obtained from both regularization methods indicate the presence of a copper-bearing zone in the southern section and another in the northern section, with an approximately west–east trend. Figs. 7a and 7c show the results from the Tikhonov regularization, which recovered smoother models with more gradual variations. In contrast, the inversion results obtained using the sparse regularization (Figs. 7b and 7d) produced models with stronger constraints, clearly delineating the boundaries of the probable mineralized bodies. This distinction is particularly evident in the chargeability inversion results.

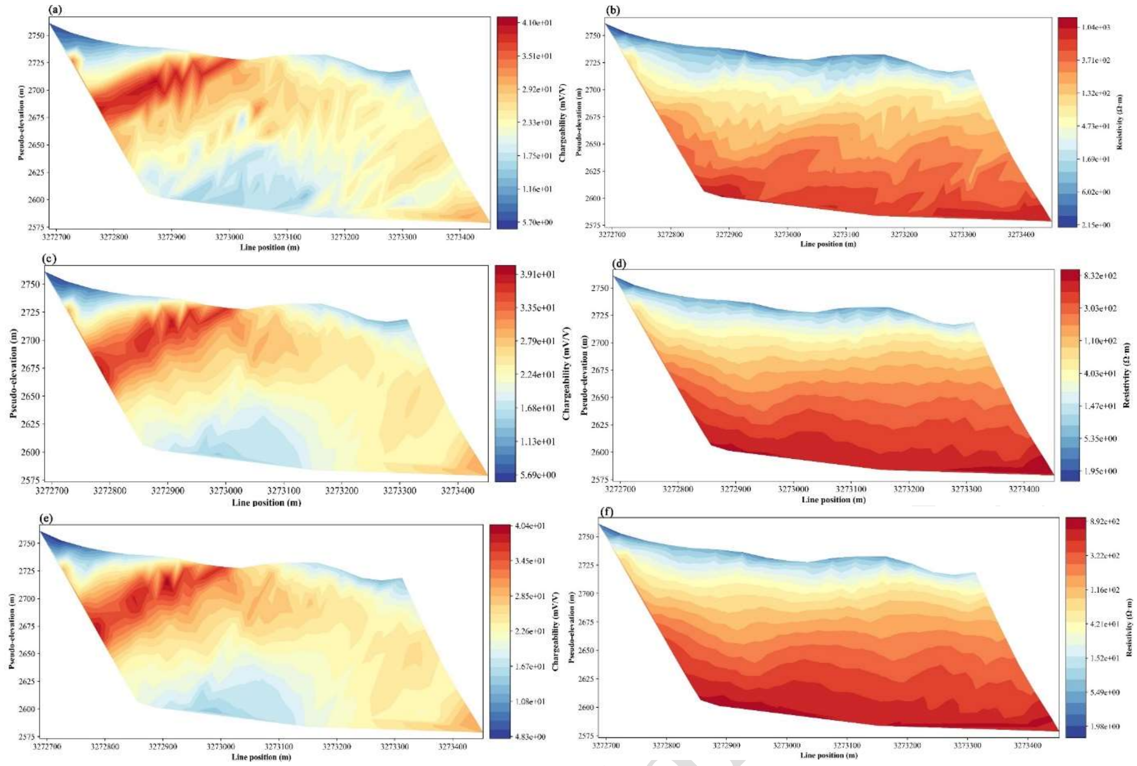

Figure 6. Comparison between observed and predicted apparent chargeability and electrical resistivity data for the study area**.** (a) Observed apparent chargeability data, (b) Observed apparent electrical resistivity data, (c) Predicted apparent chargeability data with Tikhonov regularization, (d) Predicted apparent electrical resistivity data with Tikhonov regularization (e) Predicted apparent chargeability data with Sparse regularization, (f) Predicted apparent electrical resistivity data with Sparse regularization

To further validate the geophysical results, copper grade and alteration cross-sections were utilized. In the southern section, the dominant alterations include sericite–quartz and argillic assemblages, which are likely associated with sulfide mineralization, predominantly pyrite with minor chalcopyrite (Fig. 7f). The southern copper-bearing zone extends from approximately 100 meters to nearly 250 m depth (Fig. 7e). A second anomaly extends from the central to the northern part of the profile, where strong sericite–quartz alteration is observed, coinciding with regions exhibiting high chargeability anomalies and moderate resistivity (Fig. 7f). This central–northern copper-bearing zone shows substantial lateral extension and, based on the copper grade cross-section, exhibits higher grades than the southern zone. The zone begins near the surface and continues to a depth of approximately 300 meters (Fig. 7e).

To further evaluate the quality of the chargeability inversion results, comparative plots for the two regularization methods–Tikhonov and sparse regularization—were analyzed (Fig. 8). Fig. 8a shows the variation of data misfit (ϕ_d) versus iteration number for both methods. In the early iterations, the ϕ_d values decrease rapidly and then approach a stable condition. When ϕ_d stabilizes at a low and constant level, it indicates that the inversion has achieved an optimal balance between data fitting and model stability. Both inversion methods reached stability approximately by the eighth iteration. Notably, during the initial iterations, the data misfit values obtained from sparse regularization were lower than those from the Tikhonov regularization, indicating a better early-stage data fitting performance. Fig. 8b illustrates an index representing the smoothness or complexity of the model. An increase in ϕ_m indicates a stronger influence of the sparsity constraint, resulting in a simpler and more compact model. As shown, the ϕ_m value in the sparse regularization method is higher, reflecting a greater degree of compactness in the recovered model. Fig. 8c presents the variations of the objective function, which describes the convergence behavior of the inversion. A comparison of the objective functions between the two regularization methods shows that the sparse regularization exhibits a faster reduction in the early iterations, indicating a more rapid error minimization and more effective model adjustment compared to the Tikhonov approach. Fig. 8d shows the gradual decrease in the regularization parameter (β),which controls the balance between data fidelity and model smoothness. This parameter remains consistently lower for the sparse regularization, suggesting a stronger emphasis on fitting the data. Fig. 8e demonstrates the balance achieved between data fidelity and model complexity. Fig. 8f shows an acceptable fit between the observed and predicted data for both regularization methods. Fig. 8g presents the RMS error percentage at each iteration, which stabilizes at approximately 2% for both approaches. Notably, the sparse regularization records a slightly lower RMS value during the early iterations compared to the Tikhonov method. Fig. 8h illustrates the distribution of relative errors between the observed and predicted data. The mean relative error is –0.56% for the Tikhonov method and –0.53% for the sparse regularization, indicating a normal error distribution with no systematic bias in either inversion. Finally, Fig. 8i depicts the correlation between resistivity and chargeability, which is negative (–0.30). This inverse relationship is consistent with the presence of porphyry copper mineralization within the study area.

For the quantitative evaluation of inversion performance, borehole data located near the A–B profile were used, and the results are presented in Fig. 9. Figs. 9a and 9c show the Tikhonov inversion results for electrical resistivity and chargeability, respectively. These models exhibit smooth and continuous variations with depth, resulting in broad anomalies with diffuse boundaries.

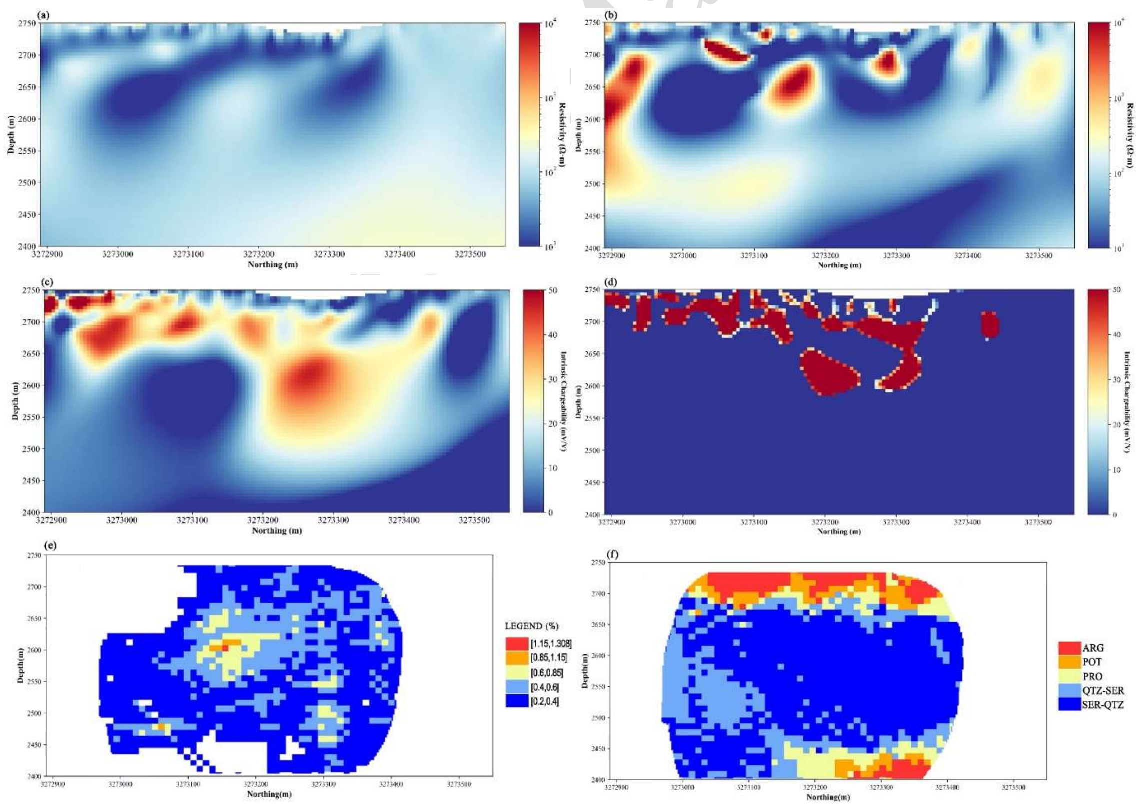

Figure 7. Geophysical and Geological characteristic of Cu porphyry deposit along profile A-B, (a) Electrical resistivity inversion section with Tikhonov regularization, (b) Electrical resistivity inversion section with sparse regularization, (c) Electrical chargeability inversion section with Tikhonov regularization, (d) Electrical chargeability inversion section with sparse regularization, (e) Cu concentration for a cut-off value of 0.2 %, (f) rock alterations

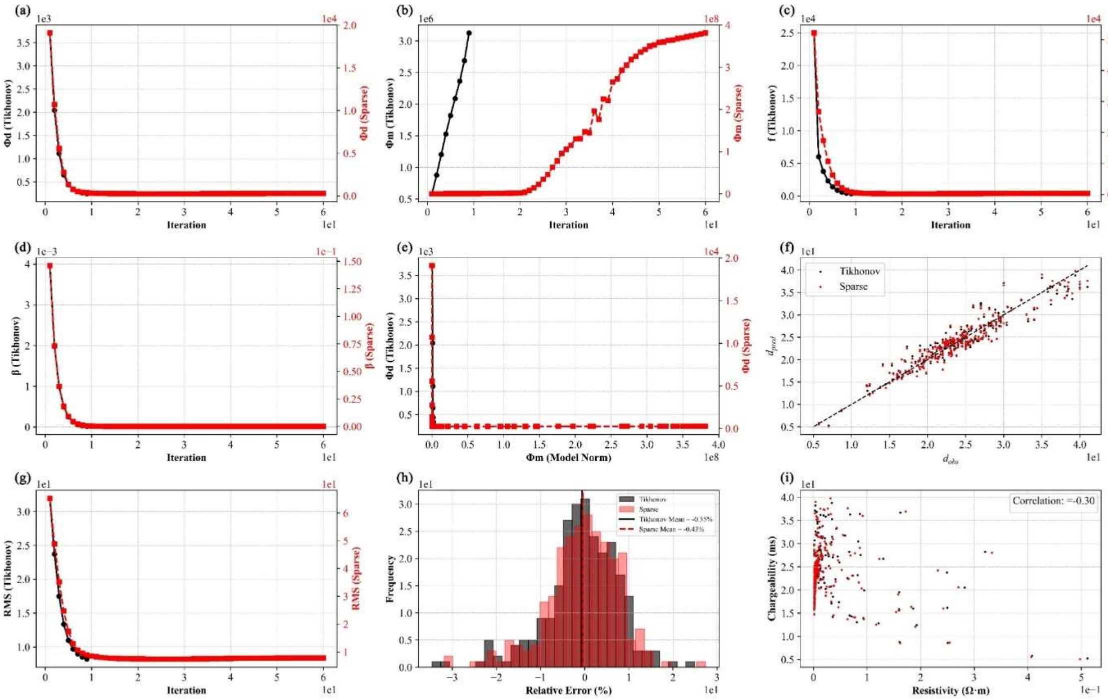

Figure 8. Quantitative evaluation of inversion performance along the A–B profile for electrical chargeability data using Tikhonov and Sparse regularization methods. (a) Data Misfit (ϕ_d), (b) Model Norm (ϕ_m), (c) Objective Function ($f = \phi_d + \beta\phi_m$), (d) Beta Schedule (β), (e) L-curve (ϕ_d vs ϕ_m), (f) Data Fit, (g) RMS error (%), (h) Histogram of Relative Error (%), (i) Scatter Plot Resistivity and chargeability data

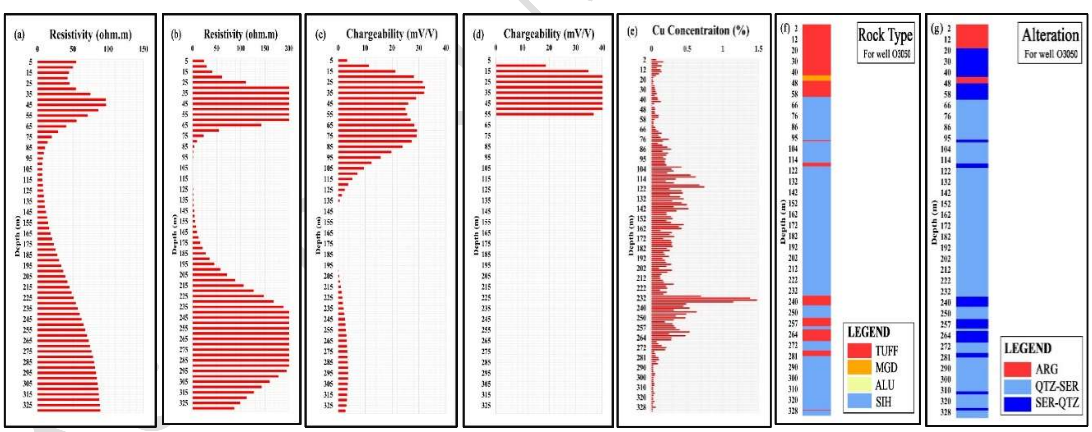

Figure 9. Drilling result at borehole O3050 (a) Electrical Resistivity using Tikhonov regularization, (b) Electrical Resistivity using Sparse regularization, (c) Electrical chargeability using Tikhonov regularization, (d) Electrical chargeability using Sparse regularization, (e) Cu Concentration, (f) rock type column, and (g) rock alteration column

This behavior is characteristic of Tikhonov regularization, which penalizes abrupt spatial variations. Although this approach effectively captures the overall trends in subsurface properties, it shows limited capability in accurately delineating layer boundaries and resolving their precise depths in this case. Figs. 9b and 9d present the results of sparsity-promoting regularization for electrical resistivity and chargeability data, respectively. The results show a marked reduction in the spatial smearing typically associated with conventional Tikhonov-based approaches. Sulfide-bearing zones are imaged in a more localized manner and exhibit higher contrast, leading to improved delineation of compact anomalies. The joint interpretation of the four inversion results together with the copper concentration column (Fig. 9e) and the alteration column (Fig. 9f) indicates that the sparsity-promoting regularization exhibits strong depth-resolving capability. In particular, the high-chargeability zone in the upper section shows a clear correspondence with argillic and sericite–quartz alteration zones. At greater depths, the increase in resistivity may reflect either lithological variations (Fig. 9f) or a transition toward more siliceous alteration zones (SIH).

Discussion

Porphyry systems typically exhibit both sharp and gradational features; therefore, they cannot be fully described using a purely sparse model. Gradational alteration zones and disseminated mineralization are more appropriately represented using smooth regularization approaches. Accordingly, sparsity-promoting inversion should not be considered a universally optimal method, but rather a complementary approach to be used alongside smooth inversion techniques, depending on the expected subsurface characteristics. A comparison between smooth (Tikhonov) regularization and sparsity-promoting regularization reveals a fundamental trade-off: smooth regularization is more suitable for representing continuous variations and diffuse structures, whereas sparse regularization is more effective in recovering compact, high-contrast anomalies. Therefore, the choice of regularization strategy should be guided by the geological context and exploration objectives, rather than by any assumption of the intrinsic superiority of either approach.

The primary objective of this study is to compare the behavior of smooth (Tikhonov) and sparsity-promoting regularization schemes under controlled conditions, rather than to demonstrate the absolute superiority of either approach. Both inversion methods are evaluated within a consistent forward modeling framework and using identical data and discretization settings to ensure a fair comparison. Synthetic models with sharp boundaries may inherently favor sparsity-promoting methods in terms of boundary recovery. However, such models are widely used in geophysical inversion studies to investigate and analyze the response of different regularization strategies to well-defined and controlled structural features. We acknowledge that the use of a synthetic model with sharp boundaries may introduce a degree of structural bias in favor of sparsity-based inversion, particularly when performance is assessed in terms of boundary sharpness. To mitigate this effect, both inversion approaches were applied under identical modeling assumptions and parameterization strategies, and the comparison was not based solely on qualitative visual assessment. Therefore, the results should be interpreted as a comparative evaluation of regularization behaviors under controlled conditions, rather than as a definitive ranking of inversion method performance.

Conclusion

In this study, a comprehensive comparative analysis was conducted between two widely used regularization techniques–Tikhonov and sparse regularization–to highlight the crucial role of regularization in enhancing the accuracy and stability of geoelectrical inversion for mineral exploration, particularly porphyry copper deposits. The comparison of these two methods, applied to both synthetic and field data from the Takhte-Gonbad porphyry copper deposit, revealed significant differences in model reconstruction. The Tikhonov method produces smooth and continuous models and exhibits stable inversion behaviour; however, it tends to attenuate sharp geological contrasts and may smear structural boundaries, thereby reducing the resolution of localized features. In contrast, sparsity-promoting regularization yields more compact models with sharper boundaries, improving the delineation of localized anomalies and structural discontinuities. These differences reflect the inherent trade-off between smoothness and sparsity constraints rather than an absolute measure of model accuracy. The inversion of real resistivity and chargeability data delineated two main mineralized zones. The southern zone, associated with sericite–quartz and argillic alterations, likely corresponds to pyrite-dominated sulfide mineralization with minor chalcopyrite. The central-to-northern zone, characterized by stronger sericite–quartz alteration and higher chargeability responses, corresponds to more intense porphyry copper mineralization extending from the surface to approximately 300 m depth. Quantitative convergence analysis indicates that sparsity-promoting regularization can achieve lower data misfits and more compact model representations than the Tikhonov approach, depending on inversion parameters and model characteristics. Differences in convergence behaviour between the two methods are also observed in certain cases. Overall, the results suggest that the sparsity-promoting approach enhances the delineation of sharp lithological boundaries and localized mineralized zones in porphyry systems. However, this improvement primarily reflects its tendency to emphasize compact structures and should be interpreted as a methodological trade-off rather than a general advantage over smooth regularization. The findings of this research provide valuable insights for geophysical exploration, emphasizing that the selection of an appropriate regularization method should be aligned with the geological characteristics of the study area and the specific exploration objectives.

Acknowledgements

The authors wish to express their heartfelt gratitude to the School of Mining Engineering at the University of Tehran for their invaluable support.

Author Contributions

M. Hosseini: Conceptualization, Methodology, Software, Formal Analysis, Investigation, Writing - Original Draft. M. Abedi: Conceptualization, Methodology, Data Provision, Review & Editing, Supervision. M. Mirmohammadi: Review & Editing, Supervision. R. Ghezelbash: Review & Editing, Advisor. B. Sadraeifar: Methodology and Software. All authors have read and agreed to the published version of the manuscript.

Data Availability Statement

Data are available upon reasonable request to the corresponding author via the email address maysamabedi@ut.ac.ir.

Competing interests

The authors declare that they have no known competing financial interests or personal relationships that could have appeared to influence the work reported in this paper.

References

Abedi, M., 2020. A focused and constrained 2D inversion of potential field geophysical data through Delaunay triangulation, a case study for iron-bearing targeting at the Shavaz deposit in Iran. Physics of the Earth and Planetary Interiors, 309: 106604.

Abedi, M., Afshar, A., Ardestani, V.E., Gholam, A., Norouzi, G.H., Lucas, C., 2010. Application of various methods for 2D inverse modeling of residual gravity anomalies. Acta Geophysica, 58: 317-336.

Afzal, P., Tehrani, M.E., Ghaderi, M., Hosseini, M.R., 2016. Delineation of supergene enrichment, hypogene and oxidation zones utilizing staged factor analysis and fractal modeling in Takht-e-Gonbad porphyry deposit, SE Iran. Journal of Geochemical Exploration, 161: 119-127.

Ardestani, V.E., Fournier, D., Oldenburg, D.W., 2022. A localized gravity modeling of the upper crust beneath central Zagros. Pure and Applied Geophysics, 179: 2365-2381.

Aster, R.C., Borchers, B., Thurber, C.H., 2018. Parameter Estimation and Inverse Problems. Elsevier.

Babaei, M., Abedi, M., Norouzi, G.H., Kazem Alilou, S., 2020. Geostatistical modeling of electrical resistivity tomography for imaging porphyry Cu mineralization in Takht-e-Gonbad deposit, Iran. Journal of Mining and Environment, 11: 143-159.

Babaei, M., Abedi, M., Norouzi, G.H., Kazem Alilou, S., 2021. 3D inverse modeling of electrical resistivity and induced polarization data versus geostatistical-based modeling. Geopersia, 11: 319-336.

Bakushinsky, A.B., Kokurin, M.M., Kokurin, M.Y., 2018. Regularization Algorithms for Ill-Posed Problems, Vol. 61. Walter de Gruyter GmbH & Co KG.

Bauer, F., Pereverzev, S., Rosasco, L., 2007. On regularization algorithms in learning theory. Journal of Complexity, 23: 52-72.

Benning, M., Burger, M., 2018. Modern regularization methods for inverse problems. Acta Numerica, 27: 1-111.

Bortolotti, V., Landi, G., Zama, F., 2025. Uniform Multipenalty Regularization for Linear Ill-Posed Inverse Problems. SIAM Journal on Scientific Computing, 47: A790-A810.

Bredies, K., Holler, M., 2020. Higher-order total variation approaches and generalisations. Inverse Problems, 36: 123001.

Calvetti, D., Somersalo, E., 2025. Distributed Tikhonov regularization for ill-posed inverse problems from a Bayesian perspective. Computational Optimization and Applications: 1-32.

Català, A., Angulo, C., 2000. A comparison between the Tikhonov and the Bayesian approaches to calculate regularisation matrices. Neural Processing Letters, 11: 185-195.

Chen, T., Zhang, G., 2018. Forward modeling of gravity anomalies based on cell mergence and parallel computing. Computers & Geosciences, 120: 1-9.

Cheng, J., Hofmann, B., Lu, S., 2014. The index function and Tikhonov regularization for ill-posed problems. Journal of Computational and Applied Mathematics, 265: 110-119.

Cockett, R., Heagy, L.J., Oldenburg, D.W., 2016. Pixels and their neighbors: Finite volume. The Leading Edge, 35: 703-706.

Cockett, R., Kang, S., Heagy, L.J., Pidlisecky, A., Oldenburg, D.W., 2015. SimPEG: An open source framework for simulation and gradient based parameter estimation in geophysical applications. Computers & Geosciences, 85: 142-154.

Dai, R., Yin, C., 2025. An iterative re-weighting algorithm for element to solve sparsity-regularized linear inverse problem and an application in sparse-spike deconvolution of seismic data. IEEE Geoscience and Remote Sensing Letters, 22: 1-5.

Doicu, A., Trautmann, T., Schreier, F., 2010. Tikhonov regularization for nonlinear problems. In: Numerical Regularization for Atmospheric Inverse Problems. Springer, pp. 163-220.

Duval, V., Peyré, G., 2017. Sparse regularization on thin grids I: the Lasso. Inverse Problems, 33: 055008.

Fakhari, S., Afzal, P., Lotfi, M., 2019. Delineation of hydrothermal alteration zones for porphyry systems utilizing ASTER data in Jebal-Barez area, SE Iran. Iranian Journal of Earth Sciences, 11: 80-92.

Fernández-Martínez, J.L., Pallero, J., Fernández-Muñiz, Z., Pedruelo-González, L.M., 2014. The effect of noise and Tikhonov's regularization in inverse problems. Part I: The linear case. Journal of Applied Geophysics, 108: 176-185.

Fernández-Muñiz, Z., Khaniani, H., Fernández-Martínez, J.L., 2019. Data kit inversion and uncertainty analysis. Journal of Applied Geophysics, 161: 228-238.

Gerth, D., 2021. A new interpretation of (Tikhonov) regularization. Inverse Problems, 37: 064002.

Gholami, A., Siahkoohi, H., 2010. Regularization of linear and non-linear geophysical ill-posed problems with joint sparsity constraints. Geophysical Journal International, 180: 871-882.

Gockenbach, M.S., 2016. Linear Inverse Problems and Tikhonov Regularization, Vol. 32. American Mathematical Society.

Golub, G.H., Hansen, P.C., O'Leary, D.P., 1999. Tikhonov regularization and total least squares. SIAM Journal on Matrix Analysis and Applications, 21: 185-194.

Gong, M., Jiang, X., Li, H., 2017. Optimization methods for regularization-based ill-posed problems: a

survey and a multi-objective framework. Frontiers of Computer Science, 11: 362-391.
Grasmair, M., Haltmeier, M., Scherzer, O., 2015. Sparsity in inverse geophysical problems. In: Handbook of Geomathematics. Springer, pp. 1659-1687.
Gupta, H., Fageot, J., Unser, M., 2018. Continuous-domain solutions of linear inverse problems with Tikhonov versus generalized TV regularization. IEEE Transactions on Signal Processing, 66: 4670-4684.
Hansen, T.M., Cordua, K.S., Jacobsen, B.H., Mosegaard, K., 2014. Accounting for imperfect forward modeling in geophysical inverse problems-Exemplified for crosshole tomography. Geophysics, 79: H1-H21.
Hassan Ibrahim, A., Kumam, P., Abubakar, A.B., Abubakar, J., Muhammad, A.B., 2020. Least-square-based three-term conjugate gradient projection method for $\ell 1$-norm problems with application to compressed sensing. Mathematics, 8: 602.
Hong, B.W., Koo, J.K., Dirks, H., Burger, M., 2017. Adaptive regularization in convex composite optimization for variational imaging problems. In: Roth, V., Vetter, T. (Eds.), Pattern Recognition. Lecture Notes in Computer Science, vol. 10496. Springer, Cham, pp. 283-296.
Hosseini, M.R., Ghaderi, M., Alirezaei, S., 2012. Mineralogy, geochemistry, involved fluids, and genesis of the Takht-e-Gonbad copper deposit, northeast of Sirjan. M.Sc. thesis, Tarbiat Modares University, Tehran, Iran.
Hosseini, M.R., Ghaderi, M., Alirezaei, S., Sun, W., 2017. Geological characteristics and geochronology of the Takht-e-Gonbad copper deposit, SE Iran: a variant of porphyry type deposits. Ore Geology Reviews, 86: 440-458.
Hu, Y., Li, C., Meng, K., Qin, J., Yang, X., 2017. Group sparse optimization via lp,q regularization. Journal of Machine Learning Research, 18: 1-52.
Huang, G., Wei, S., Gei, D., Wang, T., 2024. The $\ell 1-2$-norm-regularized basis pursuit seismic inversion based on the exact Zoeppritz equation. Geophysics, 89: R247-R260.
Huang, M.-L., Sholeh, A., Bi, X.-W., Hu, R.-Z., Pan, L.-C., Yang, Z.-Y., Zhu, J.-J., 2024. Geology and genesis of the Takht-Gonbad porphyry Cu deposit in the Kerman belt, SW Iran. Ore Geology Reviews, 175: 106395.
Jin, B., Maaß, P., Scherzer, O., 2017. Sparsity regularization in inverse problems. Inverse Problems, 33: 060301.
Jordi, C., Doetsch, J., Günther, T., Schmelzbach, C., Robertsson, J.O., 2018. Geostatistical regularization operators for geophysical inverse problems on irregular meshes. Geophysical Journal International, 213: 1374-1386.
Jupp, D., Vozoff, K., 1975. Stable iterative methods for the inversion of geophysical data. Geophysical Journal International, 42: 957-976.
Li, Q., 2023. A comprehensive survey of sparse regularization: Fundamental, state-of-the-art methodologies and applications on fault diagnosis. Expert Systems with Applications, 229: 120517.
Li, Y., Oldenburg, D.W., 1996. 3-D inversion of magnetic data. Geophysics, 61: 394-408.
Li, Y., Oldenburg, D.W., 2000. 3-D inversion of induced polarization data. Geophysics, 65: 1931-1945.
Li, Y., Oldenburg, D.W., 2003. Fast inversion of large-scale magnetic data using wavelet transforms and a logarithmic barrier method. Geophysical Journal International, 152: 251-265.
Lima, W.A., Martins, C.M., Silva, J.B., Barbosa, V.C., 2011. Total variation regularization for depth-to-basement estimate: Part 2—Physicogeologic meaning and comparisons with previous inversion methods. Geophysics, 76: I13-I20.
Lin, Y., Huang, L., 2015. Quantifying subsurface geophysical properties changes using double-difference seismic-waveform inversion with a modified total-variation regularization scheme. Geophysical Journal International, 203: 2125-2149.
Luo, X.-L., Xiao, H., Zhang, S., 2024. The regularization continuation method for optimization problems with nonlinear equality constraints. Journal of Scientific Computing, 99: 17.
Malinverno, A., 2002. Parsimonious Bayesian Markov chain Monte Carlo inversion in a nonlinear geophysical problem. Geophysical Journal International, 151: 675-688.
Mohammadi, N.M., Hezarkhani, A., 2018. Application of support vector machine for the separation of mineralised zones in the Takht-e-Gonbad porphyry deposit, SE Iran. Journal of African Earth Sciences, 143: 301-308.
Oldenburg, D.W., Li, Y., 2005. Inversion for applied geophysics: A tutorial. In: Butler, D.K. (Ed.),

Near-Surface Geophysics. Society of Exploration Geophysicists, Tulsa, Oklahoma, pp. 89-150.
Pallero, J.L., Fernández-Muñiz, Z., Cernea, A., Álvarez-Machancoses, Ó., Pedruelo-González, L.M., Bonvalot, S., Fernández-Martínez, J.L., 2018. Particle swarm optimization and uncertainty assessment in inverse problems. Entropy, 20: 96.
Ranjbar, H., Honarmand, M., Moezifar, Z., 2004. Application of the Crosta technique for porphyry copper alteration mapping, using ETM+ data in the southern part of the Iranian volcanic sedimentary belt. Journal of Asian Earth Sciences, 24: 237-243.
Ren, Z., Kalscheuer, T., 2020. Uncertainty and resolution analysis of 2D and 3D inversion models computed from geophysical electromagnetic data. Surveys in Geophysics, 41: 47-112.
Sadraeifar, B., Abedi, M., 2024. A comparative study of sparse and Tikhonov regularization methods in gravity inversion: A case study of manganese deposit in Iran. International Journal of Mining and Geo-Engineering, 58: 161-169.
Seigel, H.O., 1959. Mathematical formulation and type curves for induced polarization. Geophysics, 24: 547-565.
Selesnick, I., 2017. Sparse regularization via convex analysis. IEEE Transactions on Signal Processing, 65: 4481-4494.
Shafiei, B., Haschke, M., Shahabpour, J., 2009. Recycling of orogenic arc crust triggers porphyry Cu mineralization in Kerman Cenozoic arc rocks, southeastern Iran. Mineralium Deposita, 44: 265-283.
Silva, J.B., Medeiros, W.E., Barbosa, V.C., 2001. Potential-field inversion: Choosing the appropriate technique to solve a geologic problem. Geophysics, 66: 511-520.
Strong, D., Chan, T., 2003. Edge-preserving and scale-dependent properties of total variation regularization. Inverse Problems, 19: S165.
Tang, A., Quan, P., Niu, L., Shi, Y., 2022. A survey for sparse regularization based compression methods. Annals of Data Science, 9: 695-722.
Tikhonov, A.N., 1977. Solutions of Ill-Posed Problems. Winston and Sons, Washington, D.C.
Tinooni, S., 2021. Investigation of mineralization, alteration, and fluid inclusions of the Takht-e-Gonbad copper deposit (northeast of Sirjan, SE Iran). Iranian Journal of Crystallography and Mineralogy, 29: 35-48.
Toushmalani, R., Saibi, H., 2015. 3D gravity inversion using Tikhonov regularization. Acta Geophysica, 63: 1044-1065.
Wang, G., Chen, S., 2022. Pre-stack seismic inversion with L1−2-norm regularization via a proximal DC algorithm and adaptive strategy. Surveys in Geophysics, 43: 1817-1843.
Wang, Y., Leonov, A., Lukyanenko, D., Yagola, A., 2020. General Tikhonov regularization with applications in geoscience. CSIAM Transactions on Applied Mathematics, 1: 53-85.
Wen, F., Chu, L., Liu, P., Qiu, R.C., 2018. A survey on nonconvex regularization-based sparse and low-rank recovery in signal processing, statistics, and machine learning. IEEE Access, 6: 69883-69906.
Wright, S.J., Nowak, R.D., Figueiredo, M.A.T., 2009. Sparse reconstruction by separable approximation. IEEE Transactions on Signal Processing, 57: 2479-2493.
Xu, K., Zhong, Y., Wang, G., 2017. A hybrid regularization technique for solving highly nonlinear inverse scattering problems. IEEE Transactions on Microwave Theory and Techniques, 66: 11-21.
Yu, H., Chang, G., Zhang, S., Zhu, Y., Yu, Y., 2023. Application of sparse regularization in spherical radial basis functions-based regional geoid modeling in Colorado. Remote Sensing, 15: 4870.
Zhdanov, M.S., 2015. Inverse Theory and Applications in Geophysics, Vol. 36. Elsevier.
Zheng, P., Askham, T., Brunton, S.L., Kutz, J.N., Aravkin, A.Y., 2018. A unified framework for sparse relaxed regularized regression: SR3. IEEE Access, 7: 1404-1423.
Zhong, S., Wang, Y., Zheng, Y., Wu, S., Chang, X., Zhu, W., 2021. Electrical resistivity tomography with smooth sparse regularization. Geophysical Prospecting, 69: 1773-1789.